

Blind prediction of curved fracture surfaces in gypsum samples under three-point bending using the Discontinuous Galerkin Cohesive Zone method

Pickard, Daniel; Quinn, Christopher; Giovanardi, Bianca; Radovitzky, Raul

10.1016/j.engfracmech.2024.110205

Publication date

Document Version Final published version

Published in

Engineering Fracture Mechanics

Citation (APA)

Pickard, D., Quinn, C., Giovanardi, B., & Radovitzky, R. (2024). Blind prediction of curved fracture surfaces in gypsum samples under three-point bending using the Discontinuous Galerkin Cohesive Zone method. *Engineering Fracture Mechanics*, *306*, Article 110205. https://doi.org/10.1016/j.engfracmech.2024.110205

Important note

To cite this publication, please use the final published version (if applicable). Please check the document version above.

Copyright

Other than for strictly personal use, it is not permitted to download, forward or distribute the text or part of it, without the consent of the author(s) and/or copyright holder(s), unless the work is under an open content license such as Creative Commons.

Please contact us and provide details if you believe this document breaches copyrights. We will remove access to the work immediately and investigate your claim.

Green Open Access added to TU Delft Institutional Repository 'You share, we take care!' - Taverne project

https://www.openaccess.nl/en/you-share-we-take-care

Otherwise as indicated in the copyright section: the publisher is the copyright holder of this work and the author uses the Dutch legislation to make this work public.

FISFVIFR

Contents lists available at ScienceDirect

Engineering Fracture Mechanics

journal homepage: www.elsevier.com/locate/engfracmech



Blind prediction of curved fracture surfaces in gypsum samples under three-point bending using the Discontinuous Galerkin Cohesive Zone method

Daniel Pickard a,b, Christopher Quinn c,b, Bianca Giovanardi d,e, Raul Radovitzky a,b,*

- a Department of Aeronautics and Astronautics, Massachusetts Institute of Technology, 77 Massachusetts Ave, Cambridge, 02139, MA, USA
- ^b Institute for Soldier Nanotechnologies, Massachusetts Institute of Technology, 500 Technology Square, Cambridge, 02139, MA, USA
- ^c Center for Computational Science and Engineering, Massachusetts Institute of Technology, 77 Massachusetts Ave, Cambridge, 02139, MA, USA
- d Faculty of Aerospace Engineering, Delft University of Technology, Delft, The Netherlands
- e Delft Institute for Computational Science and Engineering, Delft University of Technology, Delft, The Netherlands

ARTICLE INFO

Keywords: Mixed-mode fracture Discontinuous Galerkin finite elements Cohesive zone models

Additively manufactured samples

ABSTRACT

A computational framework based on a Discontinuous Galerkin (DG)/Cohesive Zone formulation is utilized to simulate the experiments of the Purdue Damage Mechanics Modeling Challenge. The inelastic response of the additively-manufactured gypsum material used in the experimental tests is modeled via a dilatational plasticity model. The constitutive and fracture model parameters are calibrated using the load–displacement curves corresponding to three-point bending tests initially provided by the Challenge organizers. The test samples contained initial notches especially designed to force specific types of mixed fracture modes. The calibrated computational modeling framework is used to blindly simulate the more complex configuration of the Challenge experiments. The numerical predictions of the load–displacement curve and the shape of the curved fracture surface are compared to the experimental data provided *a posteriori*. It is found that the computational method is able to quantitatively describe the fracture response of the material including crack propagation, plastic wake, and the curved geometry of the fracture surface that results from the evolving fracture mode mixity with significant fidelity.

1. Introduction

Despite significant and continuous progress, the high-fidelity computational modeling of fracture propagation in realistic scenarios remains an ongoing and complex challenge. For this reason, collaborative research efforts have emerged with the objective to assess the state-of-the-art of computational models of fracture, and their ability to describe a variety of experiments representative of realistic settings. These initiatives include the so-called *Sandia Fracture Challenges*, whose first edition was held in 2012 [1–3]. More recently, Purdue University together with the Lawrence Livermore and Sandia National Laboratories proposed the *Purdue Damage Mechanics Challenge* 2022 [4] as an exercise to determine future directions to improve the community's ability to simulate crack formation and evolution in natural and engineered brittle–ductile materials. In this paper, we present the response of our MIT / TU Delft team to the Purdue Damage Mechanics Challenge.

As part of the Challenge, participants were provided with extensive data on several fracture experiments of additively-manufactured gypsum specimens [5]. Participants were asked to calibrate their computational models based on the experimental

E-mail address: rapa@mit.edu (R. Radovitzky).

^{*} Corresponding author at: Department of Aeronautics and Astronautics, Massachusetts Institute of Technology, 77 Massachusetts Ave, Cambridge, 02139, MA, USA.

data, and then to apply the calibrated models to provide blind predictions on the fracture response in a different, more complex experimental configuration. It bears emphasis that the predictions were truly *blind*, i.e. only the geometry and loading were disclosed to the participants, and no qualitative nor quantitative results from the actual physical experiment were released until all participants had submitted their computational predictions.

The experiments for calibration included material characterization tests (ultrasonic measurements, unconfined compressive strength, and Brazilian tests), which were intended to provide basic elastic, inelastic and fracture properties, as well as three-point bending tests with different initial notches to force specific types of crack nucleation and propagation paths. Specifically, by modifying the offset of the notch with respect to the specimen centerline, and its orientation with respect to the cross section, fracture propagation under mode I, mixed I–II, and I–III modes were induced. Five repetitions of each type of experiment provided some quantitative idea of the experimental variability. For each of the samples tested, participants were given load–displacement curves, digital image correlation data showing the crack path as a function of load, 3D X-ray tomography data with the reconstructions of the final crack surface geometry, and laser profilometries of crack surface roughness.

The configuration for the prediction Challenge incorporated the additional complexity of a triple combination of mode mixity of the I, II, and III types. This was achieved by creating a notch in the three-point bending test that was off-center, at an angle with respect to the cross section of the beam, and that had a variable height through the sample thickness. Participants were challenged to model this experiment using their preferred computational approach and they were asked to provide predictions of the load-displacement curve, the position of the crack tip (or tips, in case of multiple cracks) as a function of load and displacement, and the displacements of the front and back faces of the sample, from initial loading through post-peak failure. Finally, a bonus question asked to provide additional information on the post-mortem geometry of the two fracture surfaces.

Modeling the experiment in the challenge configuration therefore required the description of the potentially inelastic, large-deformations of the specimen, but the most critical requirement was the ability to model crack evolution from initiation until complete failure. In particular, the conditions of the Challenge configuration could give rise to complex crack geometries, including curved fracture paths and crack branching and coalescence. In addition, the inherently three-dimensional nature of the problem called for an efficient, high-performance computing algorithm able to describe the multiscale fields with sufficient resolution in a reasonable time.

A number of well-established computational approaches are available to describe fracture propagation, each exhibiting specific advantages and limitations depending on the type of damage problem at hand. Cohesive Zone Models (CZM) characterize cracks as sharp discontinuities that are resisted by cohesive tractions in the vicinity of the crack tips. Pioneered in [6,7], these models have been extensively employed due to their robust foundation in fracture mechanics and their seamless integration as interface elements within finite element frameworks. The extended finite element method (XFEM) [8,9] has the advantage of allowing cracks to form and propagate arbitrarily through the mesh. Crack propagation in XFEM can be modeled via linear elastic fracture mechanics [8,9], Cohesive Zone Models [10], or phase-field models [11]. However, XFEM methods have not furnished large-scale simulations in 3D scenarios due to scalability issues [12,13]. Alternative approaches describe cracks as diffuse interfaces where material gradually transitions from a healthy state to a fully damaged state. Popular approaches of this kind, such as continuum damage models [14] and phase-field models [15], have been very effective in describing intricate fracture paths in arbitrary geometries. However, these diffuse-interface approaches do not provide an explicit description of the crack opening geometries, which can only be estimated during post-processing.

Building upon our MIT/TU Delft team's experience in the original development and subsequent refinements of the hybrid Discontinuous Galerkin/Cohesive Zone Model (DG/CZM) framework [12,16–20], and its implementation for large-scale simulation in our research code **EMIT** [21], we have tackled the Challenge with this computational fracture mechanics approach. Key features of our approach include its ability to resolve intricate fracture paths and provide quantitative descriptions of crack opening displacements, while also exhibiting massive parallel scalability. These features, which have been demonstrated in a variety of applications, spanning from ballistic impact on ceramic plates [12] to explosive decompression of airliner fuselages [18] and fluid-driven fracture [19,20], make the DG/CZM approach an excellent candidate to address the modeling requirements of the Challenge. The DG/CZM approach is rooted in a discontinuous finite element discretization of the solid mechanics equations, as outlined in [22]. Within this framework, the displacement field is allowed to exhibit discontinuities at the boundaries of the finite elements. Prior to fracture, the solution's compatibility across element boundaries is maintained via variationally-consistent interface tractions. These, also known as fluxes in DG jargon, are replaced by a material-specific traction–separation law (TSL) describing fracture processes at the onset of fracture. Importantly, this transition occurs without introducing topological changes in the finite element mesh, even as cracks and fragments develop. This indistinctive treatment of cracked and uncracked interfaces facilitates a neat and highly-scalable parallel implementation, as demonstrated in [17], where billion-degree-of-freedom explicit dynamics fracture simulations are conducted on thousands of processors.

In order to describe distributed inelastic deformations in gypsum under the conditions of the Challenge, we adopt a variational formulation of dilatational plasticity as presented in [23] but with a non-zero yield point under deviatoric loads and linear hardening under continued deformation. We advance the system in time using a modified version of the explicit Newmark scheme. This adaptation incorporates dynamic relaxation to attain equilibrium within the quasi-static regime, while also allowing dynamic effects in case of unstable crack propagation.

A systematic approach was followed to calibrate the computational model to the experiments. We first determined the elastic material parameters so as to replicate the linear load–displacement response of the mode I experiments. We then calibrated the plasticity model parameters using the unconfined compression strength tests. Next, we calibrated the critical fracture stress and the

fracture energy release rate required by the CZM to match the load–displacement curves of the mode I, three-point bending tests. Finally, a similar approach was used to calibrate the mode mixity parameter in the CZM to the mixed-mode experiments.

The calibrated computational model was then applied to simulate the experiments with the specific geometry and loading prescribed in the Challenge configuration. After the release of the experimental test data [24], the simulation results were quantitatively compared against them following the requirements of the Challenge. In this paper, we report the results of that comparison focusing on the ability of the proposed computational framework to capture the details of the fracture response.

The structure of the paper follows the guidance provided by the organizers. In Section 2, we outline the key features of our computational framework, including the DG/CZM formulation, the adaptive time-stepping procedure, and the constitutive models employed. We then present the specialization of the approach to the calibration experiments and the material model parameter calibration procedure. In Section 3.2, we present and discuss the results obtained in the calibration and in the challenge configuration. Finally, the findings and contributions of this work are summarized in Section 4.

2. Approach information

2.1. The team

The proposing team comprises two graduate students, Daniel Pickard and Christopher Quinn, who are conducting their doctoral studies at MIT under the supervision of Prof. Raúl Radovitzky, and Prof. Bianca Giovanardi from TU Delft. The team has worked together previously in a number of different areas of research in Computational Mechanics and in modeling fracture using the DG/CZM method. It is important to emphasize that the graduate students' contribution to this Challenge was work they did in addition to their main research projects.

2.2. Numerical approach

2.2.1. Discontinuous Galerkin/Cohesive Zone modeling framework

For completeness, we summarize the DG/CZM framework for solid and fracture mechanics from [12]. Further details may be found in that reference. The weak formulation of linear momentum balance is:

$$\int_{\Omega_{0}} \rho_{0} \mathbf{B} \cdot \delta \boldsymbol{\varphi} \, dV + \int_{\partial_{N} \Omega_{0}} \mathbf{T} \cdot \delta \boldsymbol{\varphi} \, dS = \int_{\Omega_{0}} \left(\rho_{0} \ddot{\boldsymbol{\varphi}} \cdot \delta \boldsymbol{\varphi} + \mathbf{P}(\mathbf{F}; \mathbf{Q}) : \nabla_{0} \delta \boldsymbol{\varphi} \right) dV + \\
\underbrace{\int_{\partial_{I} \Omega_{0}} (1 - \alpha) \left[\delta \boldsymbol{\varphi} \right] \cdot \langle \mathbf{P}(\mathbf{F}; \mathbf{Q}) \rangle \cdot \mathbf{N}^{-} dS}_{\text{DG Consistency}} + \underbrace{\int_{\partial_{I} \Omega_{0}} (1 - \alpha) \left[\boldsymbol{\varphi} \right] \langle \mathbb{C} \nabla_{0} \delta \boldsymbol{\varphi} \rangle \cdot \mathbf{N}^{-} dS}_{\text{DG Symmetrization}} + \\
\underbrace{\int_{\partial_{I} \Omega_{0}} (1 - \alpha) \left[\delta \boldsymbol{\varphi} \right] \otimes \mathbf{N}^{-} : \langle \frac{\beta_{s}}{h_{s}} \mathbb{C} \rangle : \left[\boldsymbol{\varphi} \right] \otimes \mathbf{N}^{-} dS}_{\text{DG Stability}} + \underbrace{\int_{\partial_{I} \Omega_{0}} \alpha \mathbf{T} \left(\left[\boldsymbol{\varphi} \right], \mathbf{Q} \right) \cdot \left[\delta \boldsymbol{\varphi} \right] dS}_{\text{Charge Levy}} \tag{1}$$

In Eq. (1), φ is the discretized deformation mapping and primal unknown field, $\delta \varphi$ are its first variations, $\mathbf{P}(\mathbf{F}; \mathbf{Q})$ is the first Piola–Kirchhoff stress tensor, $\mathbf{F} = \nabla_0 \varphi$ is the deformation gradients tensor, \mathbf{Q} denotes a suitable set of internal state variables, $\mathbb{C} = \frac{\partial \mathbf{P}}{\partial \mathbf{F}}$ are the material tangents, ρ_0 is the reference mass density, \mathbf{B} is the body force vector field per unit mass, and $\tilde{\mathbf{T}}$ are the externally-imposed tractions defined over the Neumann boundary $\partial_N \Omega_0$.

The first line of this equation contains standard finite element integrals over the reference discretized domain Ω_0 , representing the virtual work of the applied body forces and surface tractions, the inertia forces, and the internal stresses. The remaining terms contain surface integrals defined over the set of interior interfaces $\partial_I \Omega_0$ between adjacent elements, which result from the discontinuous shape functions utilized to interpolate φ . In these integrals, $[\cdot]$ and $\langle \cdot \rangle$ are, respectively, the jump and average operators across the interface, whose normal in the reference configuration is N^- . The inclusion of the parameter α enables the modeling of fracture along any particular element interface in the mesh. Prior to fracture initiation, α is equal to zero at all interelement boundaries, and the first three DG surface integrals are included in the formulation. The integrals labeled DG consistency and DG symmetrization arise directly from the problem's variational structure [22,25], and are responsible for enforcing linear momentum balance at the interface prior to fracture. The DG stability term is necessary to weakly enforce compatibility and obtain a practical numerical scheme [26]. In that term, β_s is the stability factor, and h_s is a characteristic mesh size. Upon satisfaction of a critical fracture stress on both sides of a finite element quadrature point the binary variable α is set to one, which replaces the consistency, symmetrization and stabilization terms with the virtual work of the cohesive tractions $T([\![\varphi]\!], \mathbb{Q})$. The cohesive law models the degradation of the material's ability to sustain internal tractions as the interface opens up, at which point the traction vector T vanishes, and the interface becomes a new traction-free boundary. In this approach any interior interface in the mesh is permitted to fracture in this manner and therefore crack paths are limited only by the fineness of the computational mesh. In addition, the cohesive tractions resist the opening of the crack and therefore introduce a material fracture energy into the model, which is fully expended when the interface is fully fractured. The inclusion of a fracture energy endows the framework with a material length scale, which is essential in the modeling of size effects in brittle solids.

2.2.2. Numerical solution procedure

The finite element discretization of the DG/CZM equations (1) defines the following semi-discrete system of ordinary differential equations governing the time evolution of the system:

$$\mathbf{M}\mathbf{a}_{h} = \mathbf{R}(\mathbf{u}_{h}). \tag{2}$$

In Eq. (2), \mathbf{u}_h and \mathbf{a}_h are the displacement and acceleration at the discretization nodes, \mathbf{M} is the lumped mass matrix, and $\mathbf{R}(\mathbf{u}_h) = \mathbf{F}^{\text{ext}} - \mathbf{F}^{\text{int}}(\mathbf{u}_h)$, where $\mathbf{F}^{\text{int}}(\mathbf{u}_h)$ and \mathbf{F}^{ext} are the vectors representing the nodal internal and external forces, respectively.

In consistency with the experimental conditions, the system is driven by a quasi-statically applied load, as described in more in detail in Section 2.3. Consequently, the nodal accelerations in Eq. (2) are expected to be negligible, at least prior to the initiation of fracture. Nevertheless, once fracture initiation occurs, we anticipate the possibility of unstable crack propagation. To account for this scenario, we use an adaptive time integration scheme that dampens the dynamic effects in the quasi-static regime, while allowing the build-up of kinetic energy during unstable crack propagation.

More specifically, we employ a modified dynamic relaxation approach, drawing inspiration from Underwood [27]. The dynamic relaxation method is an explicit iterative technique for solving quasi-static problems based on the fundamental concept that the solution to a quasi-static problem is the steady-state solution to a fictitious dynamic problem. The classical dynamic relaxation solver therefore integrates a dynamic problem repeatedly until a steady-state condition is achieved, that is $\mathbf{R}(\mathbf{u}_h) = \mathbf{0}$. To accelerate the convergence to this steady-state, the method introduces a numerical damping term $\mathbf{C}\mathbf{v}_h$ into Eq. (2), reformulating it as follows:

$$\mathbf{M}\mathbf{a}_h + \mathbf{C}\mathbf{v}_h = \mathbf{R}(\mathbf{u}_h),\tag{3}$$

where \mathbf{v}_h is the nodal velocity, and \mathbf{C} is a damping matrix of the form $\mathbf{C} = c\mathbf{M}$. The scalar c is a damping coefficient that can be prescribed so that the steady-state solution is obtained as quickly as possible [27].

We solve Eq. (3) with a predictor–corrector scheme. We consider a time step Δt and we denote with \bullet^n the value of \bullet at time $t^n = t^{n-1} + \Delta t$. We employ the optimal mass scaling of Underwood [27] in our selection of the mass matrix \mathbf{M} and the time step Δt . Given \mathbf{u}_h^n , \mathbf{v}_h^n , and \mathbf{a}_h^n , the predictor step consists of computing a prediction of the displacement at time t^{n+1} and a prediction of the velocity at time $t^n + \frac{1}{2}\Delta t$:

$$\mathbf{u}_{h}^{n+1} = \mathbf{u}_{h}^{n} + \Delta t \ \mathbf{v}_{h}^{n} + \frac{1}{2} \Delta t^{2} \ \mathbf{a}_{h}^{n},$$

$$\mathbf{v}_{h}^{n+\frac{1}{2}} = \mathbf{v}_{h}^{n} + \frac{1}{2} \Delta t \ \mathbf{a}_{h}^{n}.$$
(4)

The corrector step computes the new acceleration and velocity:

$$\mathbf{a}_{h}^{n+1} = \frac{1}{1 + \frac{1}{2}c^{n+1}\Delta t} \left(\mathbf{M}^{-1} \mathbf{R} (\mathbf{u}_{h}^{n+1}) - c^{n+1} \mathbf{v}_{h}^{n+\frac{1}{2}} \right),$$

$$\mathbf{v}_{h}^{n+1} = \mathbf{v}_{h}^{n+\frac{1}{2}} + \frac{1}{2}\Delta t \mathbf{a}_{h}^{n+1}.$$
(5)

Alternating sequences of predictor and corrector steps are repeated until the finite element residual is sufficiently small. We introduce the following two modifications to this technique: (1) the applied load is incremented during the iterative process and (2) we adaptively select the numerical damping coefficient c^{n+1} based on whether fracture propagation is absent, stable or unstable, as described in the following.

Phase 1: Before fracture initiation

In the absence of fracture propagation, we employ a simple smoothed-in-time estimate of the optimal damping parameter of Eq. (7) given by:

$$c^{n+1} = (1 - C_1) c^n + C_1 \bar{c}^{n+1} \tag{6}$$

where C_1 is a small parameter ($C_1 = 10^{-2}$), and \bar{c}^{n+1} is a variant of the optimal damping parameter prescribed by Underwood [27]:

$$\bar{c}^{n+1} = 2 \sqrt{\max \left(\frac{\mathbf{v}_h^{n+\frac{1}{2}} \cdot \left(\mathbf{R}(\mathbf{u}_h^n) - \mathbf{R}(\mathbf{u}_h^{n+1}) \right)}{\Delta t \ \mathbf{v}_h^{n+\frac{1}{2}} \cdot \mathbf{M} \mathbf{v}_h^{n+\frac{1}{2}}}, 0 \right)}.$$
 (7)

The applied load increments are held fixed during this stage of the analysis.

Phase 2: Stable fracture propagation

After crack initiation, the strong nonlinearities attendant to the fracture process make the estimate of the optimal damping parameter of Eq. (7) inapplicable. For this reason, in the quasi-static fracture regime we cease to update the damping parameter via Eq. (6) and adopt instead an equation penalizing the total kinetic energy K exponentially, so as to dampen the energy released due to fracture propagation. Specifically, we update c with the following equation:

$$c^{n+1} = (1 - C_1) c^n + C_1 \exp\left(\frac{K^{n+1}}{K^{\text{ref}}} - 1\right) c^{\text{ref}},\tag{8}$$

where K^{n+1} is the total kinetic energy at time t^{n+1} , and c^{ref} and K^{ref} denote the value of c and K at the time of fracture initiation.

Importantly, in this phase, we divide the load increment associated with the current time step by a factor $\frac{c^{n+1}}{c^{ref}}$. The effect of this adjustment is particularly important in the presence of significant kinetic energy, which corresponds to a large damping coefficient. Under this condition, the load increment per time step is effectively reduced, which facilitates convergence towards the static solution. Conversely, when the kinetic energy decreases to the order of magnitude of K^{ref} , the load step is increased to advance the simulation faster.

Phase 3: Unstable fracture propagation

Unstable fracture propagation occurs when the creation of new crack surfaces releases more kinetic energy than can be dissipated by the fracture process, leading to the accumulation of excess kinetic energy. When the fracture process becomes unstable, the damping parameter prescribed in Eq. (8) leads to excessive, unphysical damping. To address this, we apply a constant damping coefficient to traverse the unstable regime with a value

$$c^{n+1} = C_2 e^{\operatorname{ref}}. (9)$$

This ensures the effects of damping remain comparable to those introduced in the uncracked range. We have found that values of $C_2 \approx 10$ yield the best performance. Similarly to Phase 2, we also rescale the load increment by a factor $\frac{e^{n+1}}{e^{ref}}$, which is now constant and equal to C_2 .

We estimate the moment when fracture propagation transitions from stable to unstable as the first time when the time rate of change of the total elastic and total dissipated fracture energy in the simulation coincide [28]. Specifically, denoting with D the total dissipated fracture energy within the simulation, we can estimate the rate of change of the total fracture energy $\dot{D}_{\text{smooth}}^{n+1}$ and that of the kinetic energy $\dot{K}_{\text{smooth}}^{n+1}$ at time t^{n+1} with the following equations:

$$\dot{K}_{\text{smooth}}^{n+1} = (1 - C_3) \dot{K}_{\text{smooth}}^n + C_3 \frac{K^{n+1} - K^n}{\Delta t}$$
 (10)

$$\dot{D}_{\text{smooth}}^{n+1} = (1 - C_3)\dot{D}_{\text{smooth}}^n + C_3 \frac{D^{n+1} - D^n}{\Delta t}$$
(11)

and switch to Phase 3 when D_{smooth}^{n+1} first exceeds D_{smooth}^{n+1} . We found values of $C_3 \approx 10^{-3}$ yield good estimates of the transition to instability.

2.3. Defining the problem

2.3.1. A Drucker-Prager-type plasticity model for dilatant geomaterial

Following a well-established approach to model geological materials [29–31], we describe ductile damage mechanisms via a constitutive plasticity model, whereas brittle fracture is described using a cohesive model, Section 2.4.

The constitutive response of the additively manufactured Gypsum was modeled using an isotropic, finite deformation variation of the dilatational model [32], formulated within the framework of variational constitutive updates [33,34]. The yield criterion in terms of the von Mises stress q and the pressure p is:

$$q^2 + \alpha^2 (p - p_0)^2 = \sigma_0^2 \tag{12}$$

 α is defined in terms of the friction angle ϕ by $\alpha = \frac{6\sin\phi}{3-\sin\phi}$. p_0 is defined in terms of the consolidation pressure [32] by $p_0 = \frac{p_c}{2} - \frac{\alpha}{2} p_c' \Delta \epsilon^p$ where $\Delta \epsilon_p$ is the plastic increment. To provide the material with an elastic range under tension, σ_0 is defined in terms of a yield stress σ_Y and hardening parameter H by $\sigma_0 = -\frac{\alpha}{2} p_c + H \epsilon^p + \sigma_Y$. For pressure values in the range $\left[p_0, p_0 + \frac{\sigma_0}{\alpha}\right]$, where this model will be employed, the yield stress decreases with increasing hydrostatic tension [35–40]. The plastic response is supplemented with an isotropic Hencky hyperelasticity model.

2.3.2. Computational setup: Mesh and boundary conditions

In the first geometry of the calibration experiments, the notch was at the center of the specimen so as to achieve mode I fracture propagation. The second geometry consisted of an off-centered notch, leading to fracture propagation under mixed modes I and II. In the last geometry, the notch was at the center of the specimen but rotated at a 45° angle, triggering mixed-modes I and III fracture. We show two representative calibration geometries in Figs. 1 and 2 and refer the reader to Jiang et al. [5] for more details on the calibration experiments.

In the challenge configuration, the notch was off-centered, at an angle, and with a variable height through the sample's thickness, so as to trigger mixed-modes I, II, and III fracture. The geometry of the challenge configuration in presented in Fig. 3, see Jiang et al. [24] for more details.

In both the calibration and Challenge experiments, the load was applied by means of aluminum rods in contact with the specimens, see Fig. 4. While the bottom rods were held fixed, the top rod was displaced in the negative vertical direction at a constant rate of 0.03 mm/s.

The computational domain was discretized with second-order tetrahedral elements, with a high mesh density near the notch and in a large region where the cracks are expected to propagate. For illustration purposes, Fig. 5 shows the mesh corresponding to the Challenge configuration, which contained 238,000 bulk elements, and a total of 7,140,000 degrees of freedom. The different colors represent the different partitions used in the 576-CPU parallel calculation.

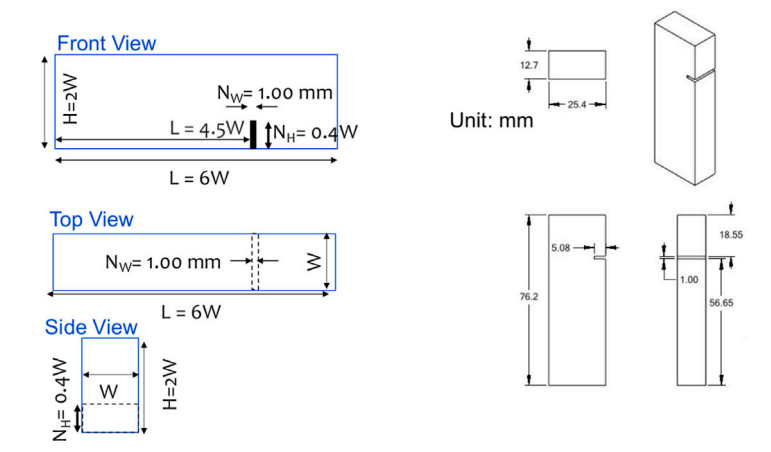


Fig. 1. Sample and notch geometry for the mixed-modes I and II fracture calibration setup. The notch is off-centered and straight through the sample's thickness.

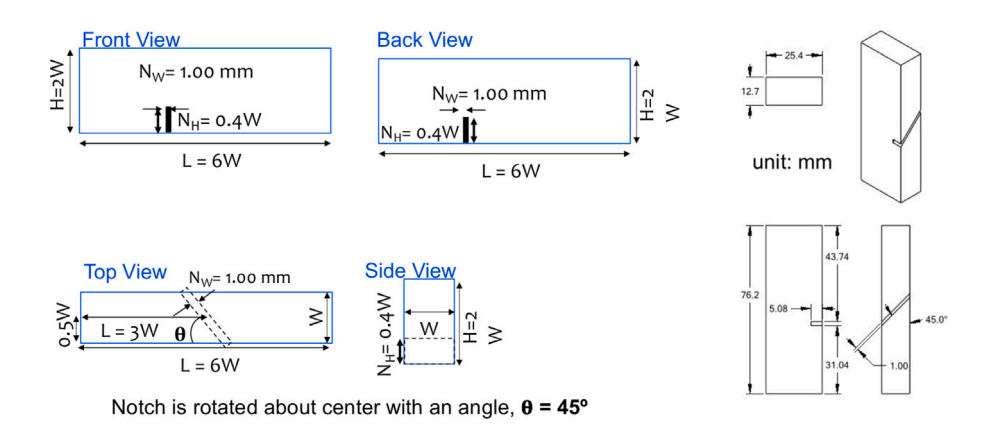


Fig. 2. Sample and notch geometry for the mixed-modes I and III fracture calibration setup. The notch is at the center of the specimen and skew through the sample's thickness.

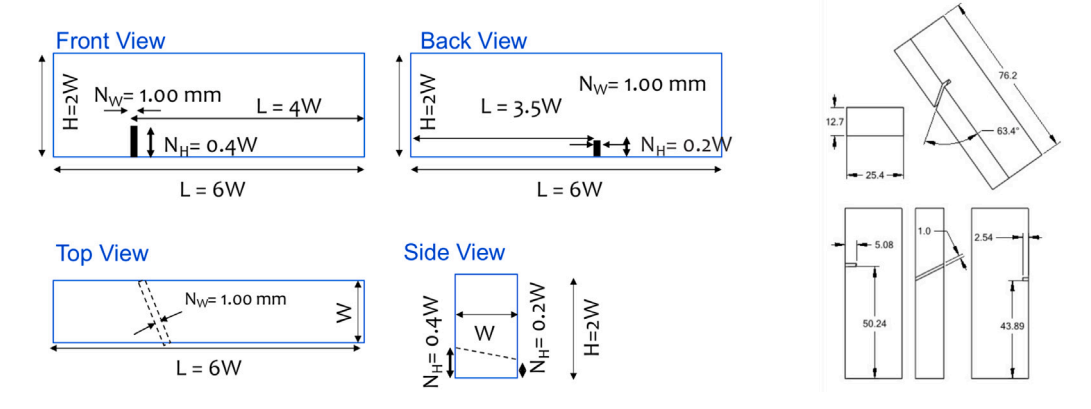


Fig. 3. Sample and notch geometry for the challenge configuration (mixed-modes I, II, and III). The notch is off-centered, skew, and with variable height through the sample's thickness.

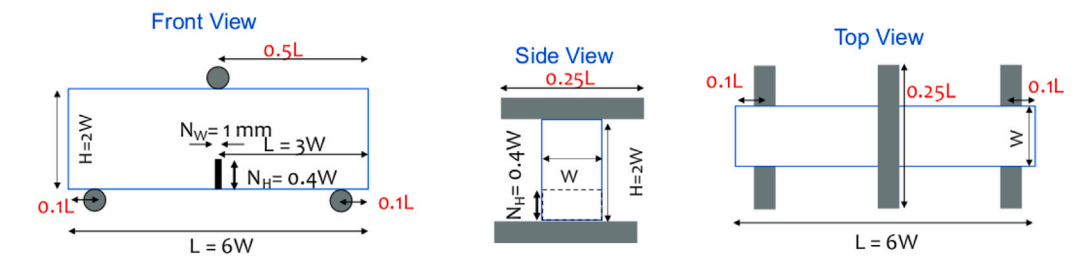


Fig. 4. Schematic of the experimental loading conditions (identical in all three-point tests in both the calibration and challenge configurations). The load is applied by means of aluminum rods placed in contact with the specimens and displaced at a constant quasi-static rate.

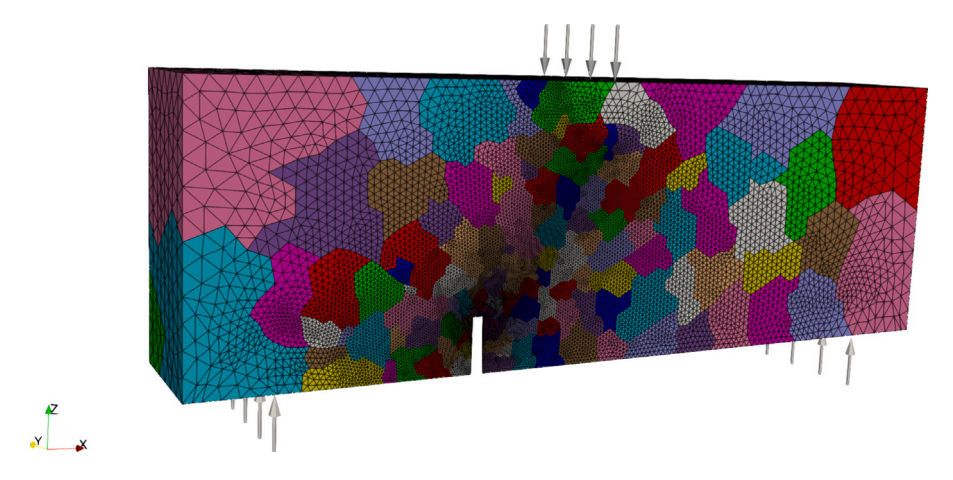


Fig. 5. Finite element mesh and mesh partition used for the challenge configuration. The mesh contains 238,000 bulk elements, and a total of 7,140,000 degrees of freedom. The different colors in the figure represent the mesh partitions used in the 576-CPU parallel calculation, where each mesh partition is assigned to one CPU.

Dirichlet boundary conditions were used to apply the external load and supports. At the top of the sample, we applied an incremental displacement in the negative z direction at an initial rate of 2.0 nm per time step. During the simulation, the imposed displacement rate was adjusted using the adaptive algorithm described in Section 2.2.2.

We employed a coarse mesh at the supports to intentionally under-resolve the unphysical singularity associated with the point load, Fig. 5. This approach helped mitigate the occurrence of spurious cracks induced by these unphysical stress concentrations. In addition, we implemented measures to prevent fracture initiation in areas adjacent to the Dirichlet nodes.

2.4. Processes & fracturing

The fracture criterion used in the Cohesive Zone Model (Section 2.2.1) is, [12]:

$$\sqrt{(\boldsymbol{\sigma}:[\mathbf{n}\otimes\mathbf{n}])^2 + \gamma^{-2}(\boldsymbol{\sigma}:[\mathbf{n}\otimes\mathbf{m}])^2} \geq \sigma_c,\tag{13}$$

where σ is the Cauchy stress and \mathbf{n} and \mathbf{m} denote, respectively, the unit normal and tangent vectors to the finite element interface in the deformed configuration. In Eq. (13), σ_c is the critical fracture stress, and the mode mixity parameter γ is the ratio of the mode II to the mode I fracture energies.

Upon satisfaction of the above fracture criterion, a traction–separation law becomes active, describing the degradation of internal traction across an interface. Following the approach outlined in [41], we decompose the displacement jump $\llbracket \varphi \rrbracket$ into its normal $\Delta_n = \llbracket \varphi \rrbracket \cdot \mathbf{n}$ and tangential $\Delta_m = \llbracket \varphi \rrbracket \cdot \mathbf{n}$ components, and we prescribe the following traction–separation law:

$$\mathbf{T}(\llbracket \boldsymbol{\varphi} \rrbracket, \mathbf{Q}) = \frac{T(\delta, \mathbf{Q})}{\delta} \left(\gamma^2 \Delta_m \mathbf{m} + \Delta_n \mathbf{n} \right), \tag{14}$$

where $\delta = \sqrt{\gamma^2 \Delta_m^2 + \Delta_n^2}$ is a scalar effective opening that enables the modeling of fracture modes coupling. In Eq. (14), $T(\llbracket \varphi \rrbracket, \mathbf{Q})$ is a scalar effective cohesive traction defined by the following expressions for loading and unloading:

$$T\left(\delta, \delta_{\max}\right) = \begin{cases} \sigma_c \left(1 - \frac{\delta}{\delta_c}\right) & \text{for } \delta \ge 0 \text{ and } \delta = \delta_{\max} & \text{(loading)} \\ \frac{T_{\max}}{\delta_{\max}} \delta & \text{for } \delta < 0 \text{ or } \delta < \delta_{\max} & \text{(unloading)} \end{cases}$$

$$(15)$$

Here, δ_c is the effective opening at complete fracture, and δ_{\max} and T_{\max} are the maximum effective opening and traction occurring over the prior history of the quadrature point. For $\delta > \delta_c$, we model complete decohesion by setting T=0. In case of crack closure $(\Delta_n=0,\dot{\Delta}_n<0)$, we model the interface traction in the normal direction by the continuum response (i.e. by reinstating the DG form of the interface terms).

2.5. Uncertainty in the model

The experiments contain a number of sources of uncertainty, the most important of which being the stochastic nature of the material response. This is a direct consequence of the variability of the microstructure arising from the additive manufacturing process. The experimental data provided did not contain sufficient information to compute quantitative statistical distributions of the model parameters, which could enable the application of modern tools of statistical inference and uncertainty quantification. As a result, no attempt was made to conduct an analysis of this type.

In addition, owing to the expense of the simulations, and the limited time and resources, no attempt was made to conduct parameter sensitivity studies.

2.6. Model calibration

Calibration of the material parameters was performed against the experiments conducted by the Challenge organizers [5]. Of the set of calibration data available, we employed the load–displacement curves of the three-point bending tests performed with the four different notch geometries, inducing crack propagation under mode I, and mixed-modes I and II, and I and III.

We utilized these load–displacement curves to calibrate the material parameters of our constitutive model. The calibration process consisted of conducting simulations of the calibration experiments adjusting the model parameters in an iterative fashion until an optimal match of the load–displacement curves between simulations and experiments was obtained. The initial values were based on simple analytical estimates of the elastic and yield response. See Section 3.1 for a more detailed discussion of the calibration methodology.

Other calibration tests provided data that appeared to be inconsistent with the data of the three-point bending tests. This included the ultrasonic measurements of elastic properties, and the uniaxial compression tests. We did not investigate the causes of the discrepancies among different types of experiments.

2.7. Model set-up and run times

The simulation framework described above was already largely implemented in our research group's software library for large-scale simulation of complex material response Σ MIT [21]. Necessary extensions included modifications to the constitutive material and fracture models, and to the load stepping adaptive approach before and after fracture as described above. All the simulations presented in this paper were conducted using specialized application drivers in C++ that invoked the Σ MIT library application programming interface (API), and orchestrated the control flow and parallel execution of the simulation. The computational domain was created with the software *gmsh* [42].

All the simulations were performed using the MIT SuperCloud [43,44], a high-performance computing cluster. The calibration and Challenge simulations required between 3 and 5 days to complete, using 12 nodes and 48 processors per node (i.e. a total of 576 processors).

2.8. Result visualization methods

Throughout the simulations, checkpoint and simulation data were dumped to unstructured parallel VTK files (vtu and pvtu) files at a given load step frequency for the purpose of restart and visualization. In addition, the reaction forces at the supports (where the displacement boundary conditions were applied) were extracted from the simulations directly from the residual forces array, collected among the pool of parallel processes using the Message Passing Interface (MPI) library, and saved to file at each load step. The data from this file was used to plot the load–displacement curves using the Matplotlib Python package [45]. We utilize Paraview [46,47] as our main visualization software. A number of scripts using the Paraview Python interface were created to extract the relevant data to produce rendered simulation scenes shown in this paper's figures.

3. Results and discussion

3.1. Matching or using the calibration data

The calibration of the finite element model was performed in a stepwise manner in which the elastic parameters were calibrated first, then the plasticity, and finally the fracture model parameters. The elastic parameters were determined using the mode I experiments. Since the results of these experiments were provided for a single orientation of the sample, we did not attempt to quantify the anisotropy in the material response and we adopted an isotropic material model. An initial estimate of the elastic modulus E=0.478 GPa was obtained from simple beam theory. It bears emphasis that this was done just for the purpose of initializing the calibration process, and is not expected to yield a good match, since beam theory assumptions are violated by

Table 1
Material model and fracture parameters.

Parameter name	Symbol	Value	Units
Young's modulus	E	0.63	GPa
Poisson's ratio	ν	0.05	
Preconsolidation pressure	p_{c0}	75	MPa
Friction angle	φ	23.2	
Reference pressure	p_{ref}	50	kPa
Reference volumetric plastic strain (log)	$ heta_{ref}^p$	0.1	
Linear hardening parameter	H	2	GPa
Yield stress	σ_0	2	MPa
Fracture strength	σ_c	3.78	MPa
Fracture energy	G_c	140	J/m^2
Mode mixity parameter	γ	1.5	,

the experimental configuration (the length-to-height ratio is about 3, the specimen has a notch, etc.) We then changed the Young's Modulus to achieve a satisfactory match with the linear rise of the load–displacement curves, which resulted in a value E = 0.63 GPa. We adopted a Poisson's ratio of value v = 0.05, to account for the large compressibility as well as the relatively large shear wave speeds reported in the acoustic wave propagation data for this additively manufactured Gypsum material.

We adopted a yield stress of $\sigma_y = 2$ MPa which is approximately 30% of the failure strength observed in unconfined compression testing. This ratio is consistent with dilatancy stress to failure stress ratios reported for a variety of geomaterials [37].

The values of the CZM parameters were calibrated to capture the peak load and post-fracture behavior of the load–displacement curves. A critical stress value of $\sigma_c = 3.78$ MPa and fracture energy value of $G_c = 140$ J/m² were obtained from the mode I tests. As it is typical in the modeling of softening material response, the model interface energy must be sufficiently large to ensure the cohesive zone can be resolved by the computational mesh [7], which guided our calibration of G_c . This parameter controls the transition to unstable propagation and sets the length scale over which crack-tip singularities are blunted by cohesive openings. As will be shown in the simulation results, this length scale exceeds the element length scale, as required for obtaining converged simulations.

The mode mixity parameter was calibrated using the load displacement curves of the mode I and II off-center notch geometries, and the mode I and III angled-notch geometries. Mode II failures are induced in the experiments by shifting the location of the notch to one side, where the shear carried by the beam is nonzero. As the notch is shifted to the side, the bending moment that is carried by tensile stress at the notch decreases in magnitude and consequently the relative importance of in-plane shear and, hence, the mode II driving force increase. By twisting the notch, the symmetry of the specimen is broken, and out of plane shear develops which drives mode III fracture propagation. The mode mixity parameter modulates the normal and tangential components of the traction between the two surfaces of the Cohesive Zone Model, and provides a simple device to characterize the relative importance of shear stresses at crack tips. A value of $\gamma = 1.5$ was found to be sufficient to capture the transition to instability and subsequent post-fracture behavior of all the calibration experiments. The final values of the parameters obtained from the calibration procedure are presented in Table 1.

The results of the model calibration process are shown in Fig. 6. The images show a comparison of the simulation vs experimental load—displacement curves for the four different type of calibration experiments. In each image, the red line represents the simulation result, whereas the four black lines are the experimental results obtained in each of the repetitions of a given experiment. The area shaded in blue are the experimental corridors or envelopes of the minimum and maximum load for each displacement. It can be seen that there is a reasonable match between the simulation and experimental results for all four experiments. There is some discrepancy in the elastic response of the load—displacement curves because the elastic parameters were calibrated using only the mode I fracture experiment. The experiments also show some apparently-elastic stiffening during loading. This could be attributed to microcrack closure, or other internal microstructural effect in the elastic response which is not captured in the model. The peak load and deflection at the peak load are found to be in excellent agreement with the experimental results. The calibration of the fracture parameters did not require a complete simulation of the post-fracture response. Consequently, some of the simulations were stopped to save computer time on our cluster.

3.2. Matching challenge data

The calibrated computational model was then applied to the Challenge configuration, as described in Section 2.3.2. Setting up this simulation was very straightforward by small modifications of the geometry file used as input to the mesh generation tool. Otherwise, the model was used without any modifications either to the formulation or the model parameters. No further assumptions were required either. In Section 3.2.1, we present the *a posteriori* comparison between the numerical model and the corresponding experiment. In Section 3.2.2, we highlight the various physical mechanisms that arise in this experiment that the numerical model helps explain.

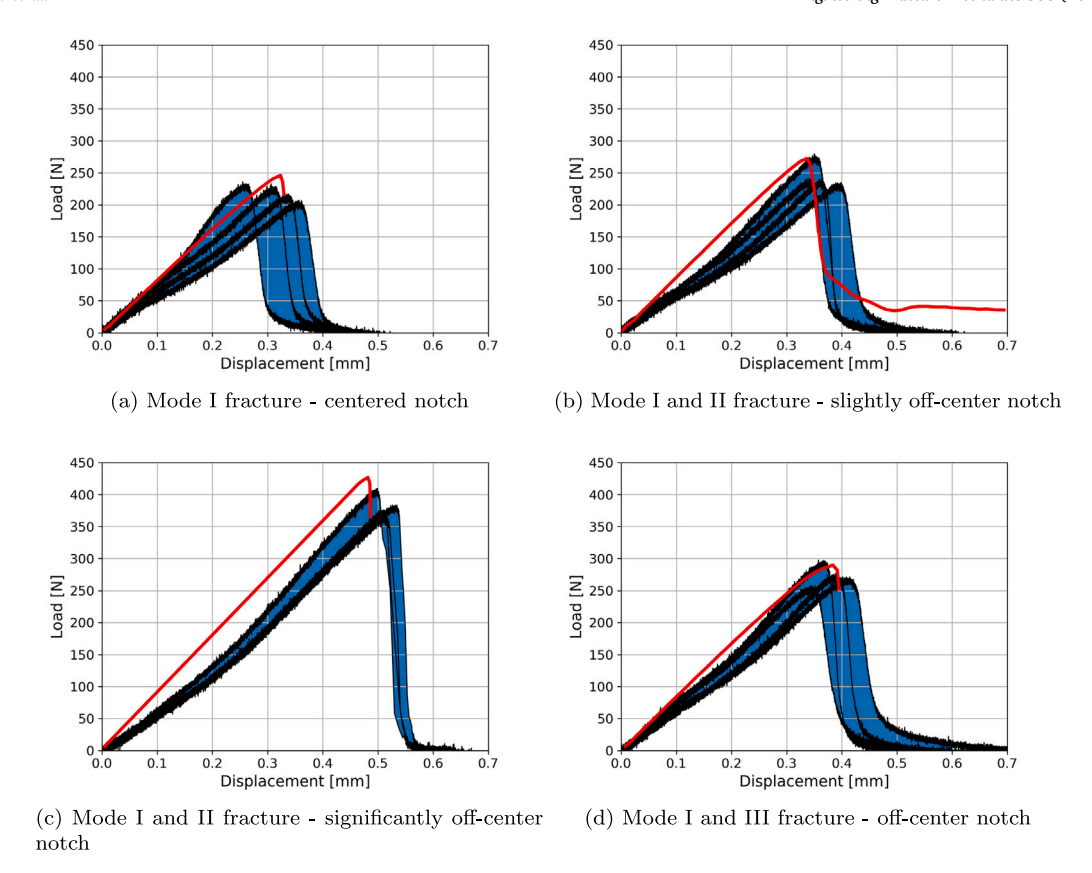


Fig. 6. Results of the model calibration process: Comparison of load displacement curves between experiments (shown in black), and the simulation result (shown in red) line. The experimental corridors are shown in the shaded blue area.

3.2.1. Comparison between simulation and experiment

The Challenge organizers provided experimental results of the three-point bending test of the final Challenge geometry after the submission of the blind prediction. The experimental results included the load–displacement curve and the fracture surface for four different experiments. The simulated load–displacement curve was found to be in excellent agreement with experimental findings up to and beyond the point of failure as shown in Fig. 7. The residual load that can be observed in the figure is due to material remaining intact near the region of application of the external load, following the measures implemented to prevent fracture initiation near the Dirichlet nodes discussed in Section 2.3.2.

In the experiments, the geometry of the fracture surfaces was obtained using laser profilometry. The sample was mounted on its side and scanned in a direction perpendicular to the cross section of the specimen of dimensions 105 mm by 200 mm, in increments of 0.1 mm. The asperity height resolution was 0.5 μ m. A mean fracture surface was computed from the data across all four repetitions of the experiment, which was then used as the basis for comparison with the geometry of the fracture surface predicted by the model. The mean fracture surface was computed by taking the mean of the x coordinate of the fracture surface $\bar{x}(y,z) = \frac{1}{4} \sum_{i=1}^4 x_i(y,z)$ at each (y,z) coordinate pair. Additionally, the range of the experimental data was computed at each position as $e(y,z) = \max_i x_i(y,z) - \min_i x_i(y,z)$, as a measure of the variability of the experimental fracture surface.

We extracted the fracture surface from the simulation by identifying the cohesive elements that had failed. We then interpolated the numerical fracture surface onto a regular grid in correspondence with the experimental data, giving the positions as values $x_h(y,z)$. A qualitative visual comparison of the geometry of the simulated vs. the experimental fracture surface for the challenge experiment is shown in Fig. 9, (see also video animation rendering in the Supplementary Information). These figures show a 3D rendering of the mean experimental fracture surface in blue, and the numerical prediction in red. The semi-transparent white lines are the edges of the finite element mesh, which were added to the visual rendering purely for the purpose of helping with the three-dimensional interpretation of the figure. The visual rendering exposes a remarkable ability of the computational model to capture the curved geometry of the experimental fracture surfaces.

A pointwise value of the error was computed by subtracting the mean fracture surface x coordinate from the numerical fracture surface x coordinate for a given (y,z) coordinate pair, i.e. $e_h(y,z) = (x_h(y,z) - \bar{x}(y,z))$. A contour plot of this local metric of the numerical error is shown in Fig. 8. It can be observed in this figure that this error remains considerably small in most regions of the cross section despite the significant complexity of the geometry of the fracture surface. There are a few small zones where the error can reach ± 1 mm, which is still quite small relative to the sample dimensions.

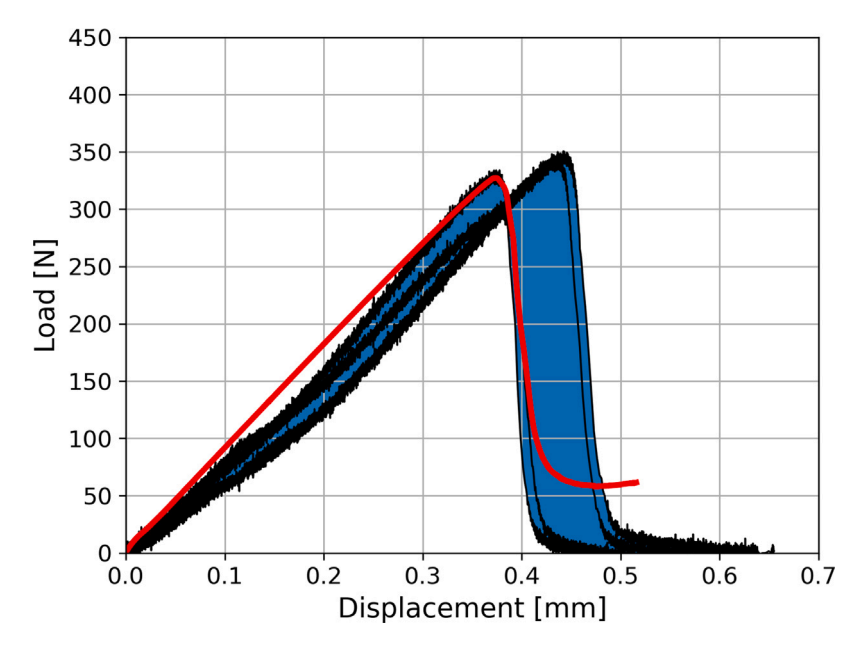


Fig. 7. Comparison of the experimental (in black) vs. simulation (in red) load-displacement curves for the three-point bending test in the final challenge geometry. The experimental corridors are shown in the shaded blue area.

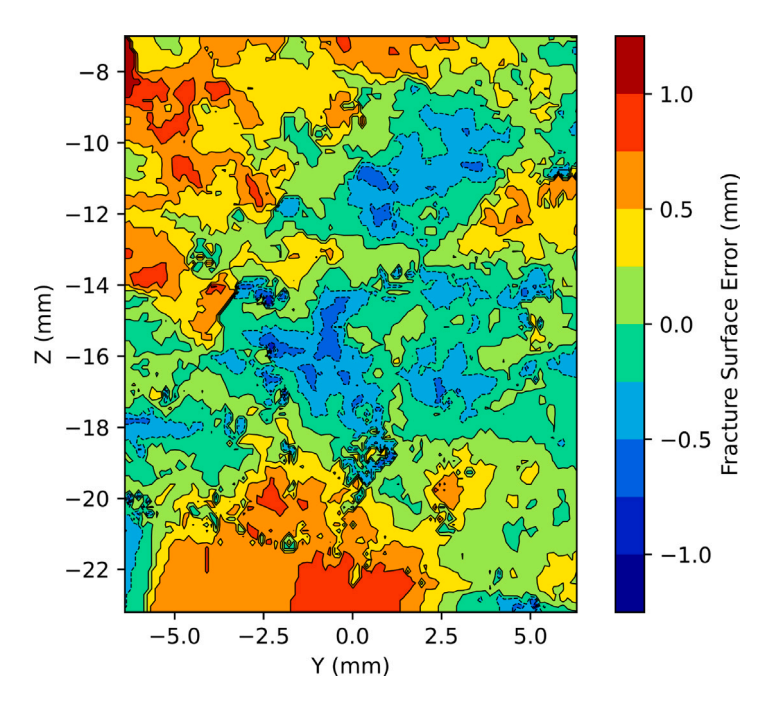
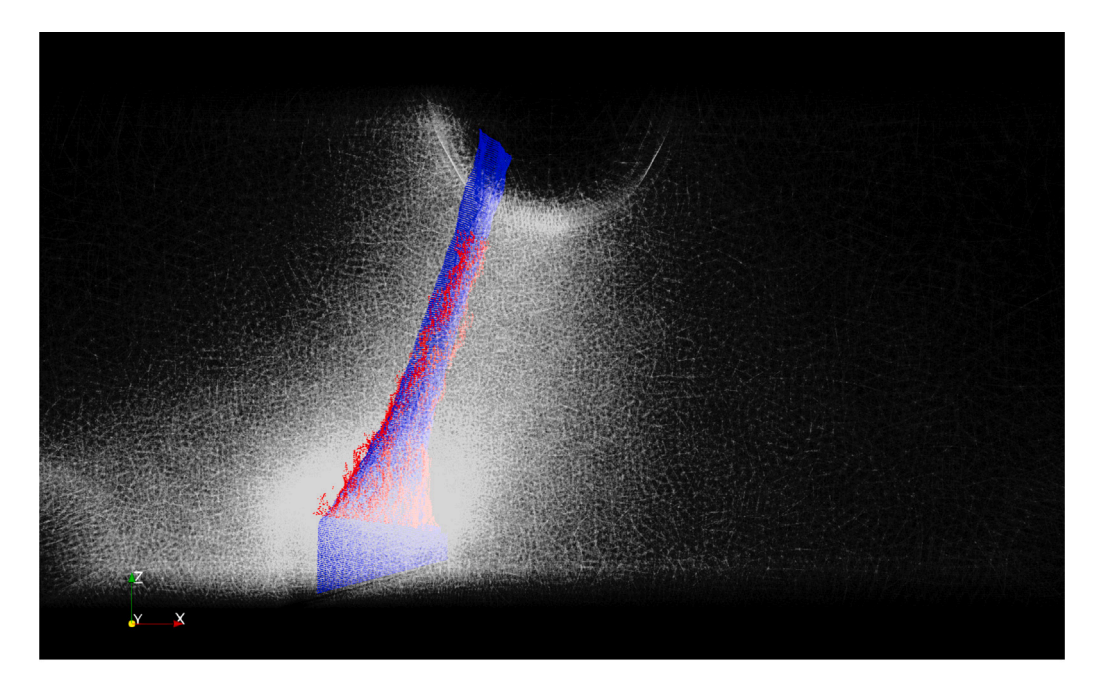


Fig. 8. Contour map of the error e_h between the predicted positions of the fracture surface $x_h(y,z)$ and the mean position of the fracture surfaces from experiments $\bar{x}(y,z)$.

To quantify the overall error of the predicted geometry of the surface, the L_2 -norm of the error with respect to the mean experimental surface was computed by a simple piecewise-constant Riemann sum. In order to obtain a relative error, this value was normalized by the L_2 -norm of the range of the experimental data, which was computed in a similar way. The normalized error obtained had a numerical value of 0.25, which indicates that the error in the geometry of the fracture surface predicted numerically is well within the bounds of the experimental variability. Further insights on the shape of the fracture surface are presented in the following subsection.



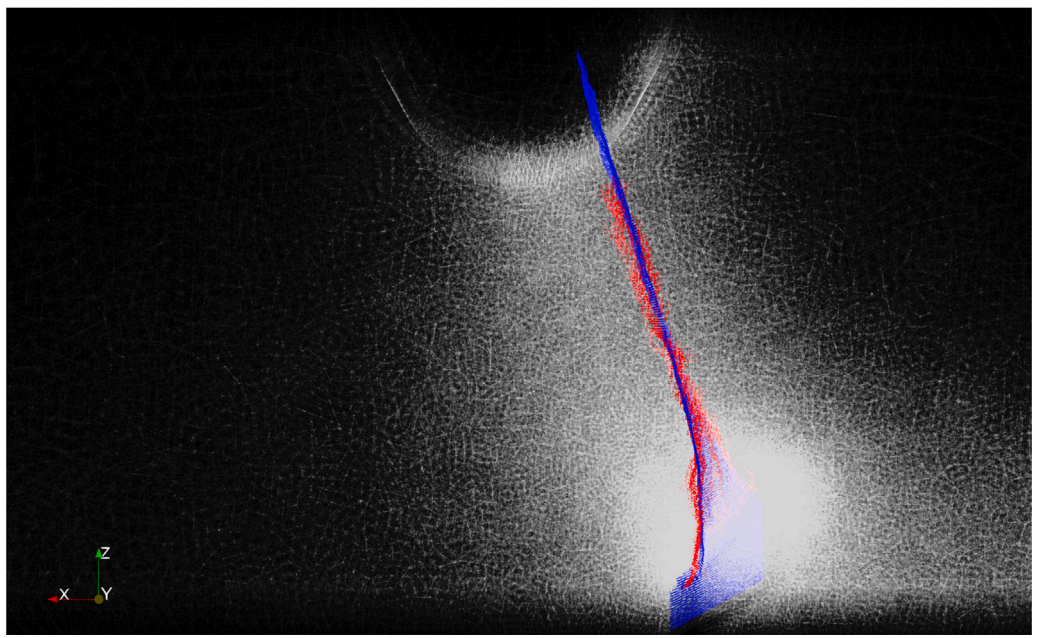


Fig. 9. Comparison of experimental and predicted geometry of the fracture surface of the blind challenge experiments (front side in top picture, back side in bottom picture). The blue dots correspond to the mean values of the location of the fracture surface across the four experimental repetitions. The red dots were interpolated from the location of the failed cohesive elements. A white, semi-transparent wireframe of the mesh is shown to aid in conveying the three-dimensionality of the problem and to contextualize the fracture surface geometry.

3.2.2. Analysis and discussion

In this section, we discuss some of the physical insights into the fracture response that the simulation of the Challenge provides. Fig. 10 shows contour plots of the von Mises stress normalized by the critical fracture stress on the front and back surfaces. This gives a sense of the evolution of the stress field as the crack progresses from the notch into the specimen. It can be observed that the stress initially intensifies at the notch corners, which causes crack nucleation. Stress intensification persists at the crack tip as it propagates through the computational domain. It bears emphasis that, in accordance with cohesive theories of fracture mechanics, the stress at the crack tip remains finite and sufficiently resolved by the finite element interpolation. The figures indicate that the region surrounding the crack tip where the stress is of the order of magnitude of the failure stress is quite large, as evidenced by the

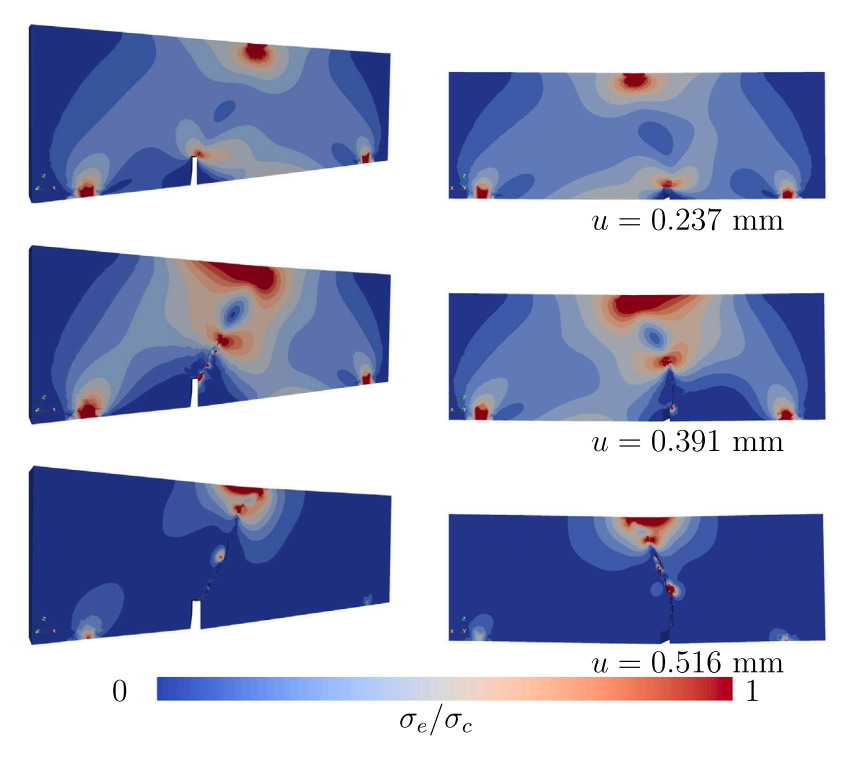


Fig. 10. Von Mises stress measure normalized by the fracture strength. The front face of the specimen is imaged on the left from an angle to portray the inclination of the initial notch. The back face is shown on the right.

large red elliptical contours emanating from either side of the advancing crack tip. This millimeter-size region corresponds to the cohesive zone which for the chosen parameters has a length scale of the order of $\frac{\pi}{8} \frac{EG_c}{(1-v^2)\sigma_c^2} = 2.4 \,\mathrm{mm}$ [48]. As the numerical model

employs smaller elements with characteristic sizes of 0.15 mm in the center of the domain, this simulation resolves the cohesive failure zone with many elements possessing several thousand degrees of freedom, which is essential for an accurate characterization of the fracture path [7].

Upon inspection of Fig. 10 at the end of the simulation, it is apparent that the crack originates at opposite sides of the width of the notch on the front and back faces of the specimen. On the front (back) face, the crack initiates from the corner of the notch closest to (farthest from) the center of the specimen. Hence, the crack path actually traverses the width of the initial notch. This is seen clearly on the right side of Fig. 11 which shows a view of the final deformed state of the notch from beneath the specimen. There are two physical mechanisms driving the traversal of the crack path across the specimen. The first is that the fracture energy required to propagate a mixed-mode fracture is larger than in pure mode I, so cracks tend towards mode I propagation. In the simulation, fracture surfaces perpendicular to the \hat{x} are energetically favorable because the stress state is dominated by tensile σ_{xx} arising from the beam's bending moment. The second effect is purely geometric and results from the decrease in energy required to drive crack propagation due to a decrease in the area of the fracture surface. These two mechanisms also cause the crack surface to twist to be nearly perpendicular to the \hat{x} direction as the fracture propagates. The curved geometry of the crack surface, both experimental and numerical, clearly shows this effect, Fig. 9.

An analysis of the evolution of the various components of the energy as the simulation progresses can also provide important insights into the stable or unstable character of the crack propagation. This has important implications on the choice of time integration algorithm, Section 2.2.2. Fig. 12 plots the logarithm of the external work, the kinetic, elastic, and dissipated fracture energies as a function of the applied displacement. In the initial stages of the simulation, there is no crack propagation, and the simulation proceeds using the scheme in Phase 1. At a deflection of about 0.07 mm, stable fracture propagation begins, and the quasi-static time integration algorithm in Phase 2 is used. It bears emphasis that this stable crack propagation persists for most of the duration of the experiment. The numerical kinetic energy is very small and remains constant during this phase. At the same time, the fracture energy rises considerably as the crack propagates along multiple element interfaces, although it remains negligible compared to the elastic energy. At a displacement of approximately 0.37 mm, the crack starts to propagate in an unstable manner. The fracture energy jumps by an order of magnitude in a very small displacement increment, whereas the elastic energy drops by almost the same amount. The kinetic energy shows large oscillations due to the sudden release of the elastic energy. This is the main reason that a different time integration algorithm is required, see Phase 3.

Finally, Fig. 13 shows contours of the volumetric plastic strain. It is clear that there is an almost imperceptible role of inelastic deformations in this experiment, which are limited to values of the order of 0.1% in the so-called plastic wake of the crack.



Fig. 11. Final fractured state viewed from beneath the specimen showing how the crack traverses the width of the notch. The top (bottom) of the figure is the front (back) of the specimen.

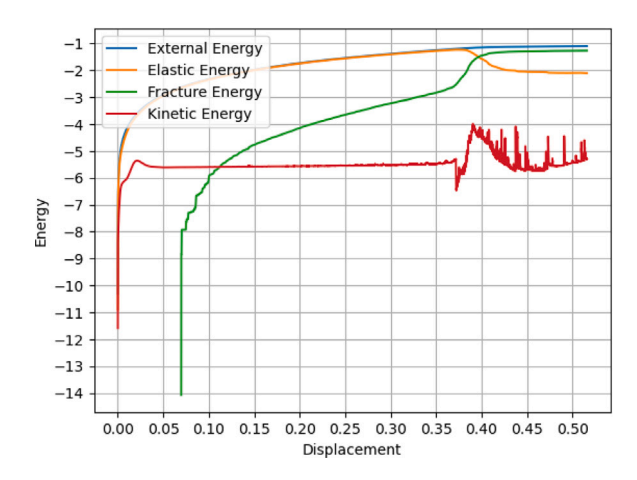


Fig. 12. Logarithmic plot of the total energy in the simulation of the three-point bending test of the final challenge geometry.

3.3. Variability

The DG/CZM approach that we adopted in our simulations restricts cracks initiation and propagation to occur only along mesh interfaces. As the mesh is refined, the set of possible fracture paths becomes richer, ultimately yielding converged crack geometries. Nevertheless, results obtained on different meshes with identical characteristic element sizes may result in fracture paths that locally may be different, but will be macroscopically equivalent. The mesh is, therefore, a source of variability inherent to our computational approach. It bears emphasis that this type of variability in the geometry of the crack is also present in the experiments. However, due to time limitations we have not investigated this or other sources of variability and we have carried out a single simulation of the challenge configuration.

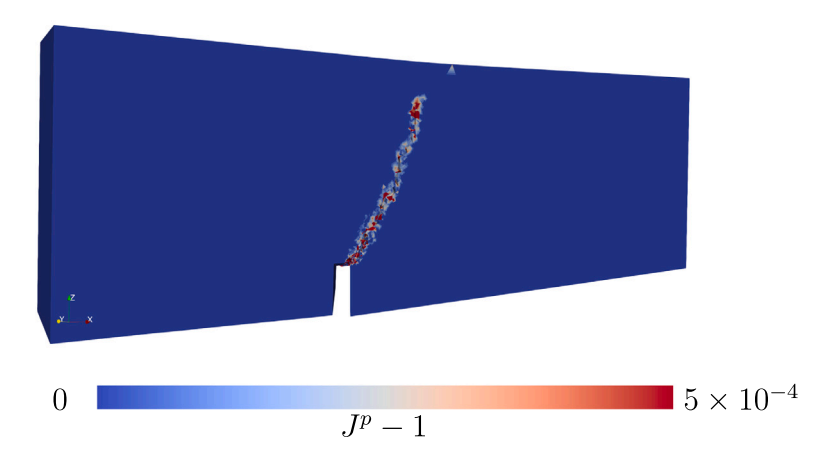


Fig. 13. Volumetric plastic strain at the end of the simulation. Note that the material in the plastic wake has dilated or expanded due to the significant hydrostatic tension induced by the crack tip.

4. Conclusions

This paper presented the response of the MIT/TU Delft team to the 2022 Purdue Damage Mechanics Challenge. The Challenge provided a rigorous framework for assessing the predictive capabilities of state-of-the-art computational models of fracture, as well as a rich dataset of well thought-out and carefully-instrumented experiments to quantify the fracture response of additively-manufactured gypsum.

Simulations of the experiments were conducted using the well-established Discontinuous Galerkin/Cohesive Zone Model (DG/CZM) computational framework, which our research group has developed and refined over many years. The framework was specialized to this problem via the implementation of gypsum-specific material models of deformation and fracture. The constitutive models were calibrated using the *ad hoc* experimental data provided by the Challenge organizers. The calibrated model was used to conduct a blind simulation of the Challenge configuration.

A quantitative comparison of the results of our simulations against the experimental data showed that the model predictions were in excellent agreement with the experiments. The model also provided important insights on the complex evolution of the curved crack path. The ability of the computational framework to predict the curved geometry of the experimental fracture surface is particularly noteworthy.

CRediT authorship contribution statement

Daniel Pickard: Writing – review & editing, Writing – original draft, Visualization, Validation, Software, Methodology, Conceptualization. Christopher Quinn: Writing – review & editing, Writing – original draft, Validation, Software, Investigation. Bianca Giovanardi: Writing – review & editing, Validation, Supervision, Software, Project administration, Methodology, Investigation, Conceptualization. Raul Radovitzky: Writing – review & editing, Validation, Supervision, Software, Resources, Project administration, Methodology, Investigation, Conceptualization.

Declaration of competing interest

The authors declare that they have no known competing financial interests or personal relationships that could have appeared to influence the work reported in this paper.

Data availability

Data will be made available on request.

Acknowledgments

The authors gratefully acknowledge support from the U.S. Army through the Institute for Soldier Nanotechnologies under Contract ARO69680-18 with the U.S. Army Research Office. B.G. gratefully acknowledges the support provided by the Delft Technology Fellowship.

Appendix A. Supplementary data

Supplementary material related to this article can be found online at https://doi.org/10.1016/j.engfracmech.2024.110205.

References

- [1] Boyce BL, Kramer SL, Fang HE, Cordova TE, Neilsen MK, Dion K, Kaczmarowski AK, Karasz E, Xue L, Gross AJ, Ghahremaninezhad A, Ravi-Chandar K, Lin SP, Chi SW, Chen JS, Yreux E, Rüter M, Qian D, Zhou Z, Bhamare S, O'Connor DT, Tang S, Elkhodary KI, Zhao J, Hochhalter JD, Cerrone AR, Ingraffea AR, Wawrzynek PA, Carter BJ, Emery JM, Veilleux MG, Yang P, Gan Y, Zhang X, Chen Z, Madenci E, Kilic B, Zhang T, Fang E, Liu P, Lua J, Nahshon K, Miraglia M, Cruce J, Defrese R, Moyer ET, Brinckmann S, Quinkert L, Pack K, Luo M, Wierzbicki T. The sandia fracture challenge: Blind round robin predictions of ductile tearing. Int J Fract 2014;186(1-2):5-68. http://dx.doi.org/10.1007/s10704-013-9904-6.
- [2] Boyce BL, Kramer SL, Bosiljevac TR, Corona E, Moore JA, Elkhodary K, Simha CH, Williams BW, Cerrone AR, Nonn A, Hochhalter JD, Bomarito GF, Warner JE, Carter BJ, Warner DH, Ingraffea AR, Zhang T, Fang X, Lua J, Chiaruttini V, Mazière M, Feld-Payet S, Yastrebov VA, Besson J, Chaboche JL, Lian J, Di Y, Wu B, Novokshanov D, Vajiragupta N, Kucharczyk P, Brinnel V, Döbereiner B, Münstermann S, Neilsen MK, Dion K, Karlson KN, Foulk JW, Brown AA, Veilleux MG, Bignell JL, Sanborn SE, Jones CA, Mattie PD, Pack K, Wierzbicki T, Chi SW, Lin SP, Mahdavi A, Predan J, Zadravec J, Gross AJ, Ravi-Chandar K, Xue L. The second Sandia Fracture Challenge: predictions of ductile failure under quasi-static and moderate-rate dynamic loading. Int J Fract 2016:198(1–2):5–100. http://dx.doi.org/10.1007/s10704-016-0089-7.
- [3] Kramer SL, Jones A, Mostafa A, Ravaji B, Tancogne-Dejean T, Roth CC, Bandpay MG, Pack K, Foster JT, Behzadinasab M, Sobotka JC, McFarland JM, Stein J, Spear AD, Newell P, Czabaj MW, Williams B, Simha H, Gesing M, Gilkey LN, Jones CA, Dingreville R, Sanborn SE, Bignell JL, Cerrone AR, Keim V, Nonn A, Cooreman S, Thibaux P, Ames N, Connor DO, Parno M, Davis B, Tucker J, Coudrillier B, Karlson KN, Ostien JT, Foulk JW, Hammetter CI, Grange S, Emery JM, Brown JA, Bishop JE, Johnson KL, Ford KR, Brinckmann S, Neilsen MK, Jackiewicz J, Ravi-Chandar K, Ivanoff T, Salzbrenner BC, Boyce BL. The third sandia fracture challenge: predictions of ductile fracture in additively manufactured metal. Vol. 218, Springer Netherlands; 2019, http://dx.doi.org/10.1007/s10704-019-00361-1.
- [4] 2023. https://purr.purdue.edu/groups/damagemechanicschallenge.
- [5] Jiang L, Pyrak-Nolte L, Yoon H, Bobet A, Morris J. Digital image, x-ray CT, XRD and ultrasonic data sets for damage mechanics challenge on brittle-ductile material. Purdue Unversity Research Repository; 2021, http://dx.doi.org/10.4231/2E8M-W085.
- [6] Ortiz M, Suresh S. Statistical properties residual stresses and intergranular fracture in ceramic materials. J Appl Mech 1993;60:77-84.
- [7] Camacho G, Ortiz M. Computational modeling of impact damage in brittle materials. Int J Solids Struct 1996;33(20-22):2899-983. http://dx.doi.org/10. 1016/0020-7683(95)00255-3.
- [8] Belytschko T, Black T. Elastic crack growth in finite element with minimal remeshing. Internat J Numer Methods Engrg 1999;45(5):601–20. http://dx.doi.org/10.1002/(SICI)1097-0207(19990620)45:5<601::AID-NME598>3.0.CO;2-S.
- [9] Moës N, Dolbow J, Belytschko T. A finite element method for crack growth without remeshing. Internat J Numer Methods Engrg 1999;46:131-50.
- [10] Moës N, Belytschko T. Extended finite element method for cohesive crack growth. Eng Fract Mech 2002;69(7):813–33. http://dx.doi.org/10.1016/S0013-7944(01)00128-X.
- [11] Giovanardi B, Scotti A, Formaggia L. A hybrid xfem-phase field (xfield) method for crack propagation in brittle elastic materials. Comput Methods Appl Mech Engrg 2017;320:396–420. http://dx.doi.org/10.1016/j.cma.2017.03.039.
- [12] Radovitzky R, Seagraves A, Tupek M, Noels L. A scalable 3D fracture and fragmentation algorithm based on a hybrid discontinuous Galerkin, cohesive element method. Comput Methods Appl Mech Engrg 2011;200:326–44. http://dx.doi.org/10.1016/j.cma.2010.08.014.
- [13] Lecampion B, Bunger A, Zhang X. Numerical methods for hydraulic fracture propagation: a review of recent trends. J Nat Gas Sci Eng 2017;49:66–83. http://dx.doi.org/10.1016/j.jngse.2017.10.012.
- [14] Chaboche J. Continuum damage mechanics: present state and future trends. Nucl Eng Des 1987;105:19–33. http://dx.doi.org/10.1016/0029-5493(87) 90225-1.
- [15] Bourdin B, Francfort GA, Marigo J-J. Numerical experiments in revisited brittle fracture. J Mech Phys Solids 2000;48(4):797–826. http://dx.doi.org/10. 1016/S0022-5096(99)00028-9.
- [16] Seagraves A, Radovitzky R. Advances in cohesive zone modeling of dynamic fracture. Springer; 2009, p. 349–405. http://dx.doi.org/10.1007/978-1-4419-0446-112, [Chapter 12].
- [17] Seagraves A, Radovitzky R. Large-scale 3D modeling of projectile impact damage in brittle plates. J Mech Phys Solids 2015;83:48–71. http://dx.doi.org/10.1016/j.imps.2015.06.001.
- [18] Talamini BL, Radovitzky R. A parallel discontinuous Galerkin/cohesive-zone computational framework for the simulation of fracture in shear-flexible shells. Comput Methods Appl Mech Engrg 2017;317:480–506. http://dx.doi.org/10.1016/j.cma.2016.12.018.
- [19] Giovanardi B, Serebrinsky S, Radovitzky R. A fully-coupled computational framework for large-scale simulation of fluid-driven fracture propagation on parallel computers. Comput Methods Appl Mech Engrg http://dx.doi.org/10.1016/j.cma.2020.113365.
- [20] Smilovich D, Radovitzky R, Dvorkin E. A parallel staggered hydraulic fracture simulator incorporating fluid lag. Comput Methods Appl Mech Engrg 384. http://dx.doi.org/10.1016/j.cma.2021.114003.
- [21] The Summit Development Group. Summit, a scalable computational framework for large-scale simulation of complex mechanical response of materials. 2023. http://summit.mit.edu.
- [22] Noels L, Radovitzky R. A general discontinuous Galerkin method for finite hyperelasticity formulation and numerical applications. Internat J Numer Methods Engrg 2006;68(1):64–97. http://dx.doi.org/10.1002/nme.1699.
- [23] Ortiz M, Pandolfi A. A variational Cam-clay theory of plasticity. Comput Methods Appl Mech Engrg 2004;193:2645–66. http://dx.doi.org/10.1016/j.cma. 2003.08.008.
- [24] Jiang L, Pyrak-Nolte L, Bobet A, Yoon H, Morris J. Challenge data set for the damage mechanics challenge. Purdue Unversity Research Repository; 2023, http://dx.doi.org/10.4231/ZX5A-OJ30.
- [25] Noels L, Radovitzky R. An explicit discontinuous Galerkin method for non-linear solid dynamics formulation, parallel implementation and scalability properties. Internat J Numer Methods Engrg 2007;74(9):1393–420. http://dx.doi.org/10.1002/nme.2213.
- [26] Arnold D. An interior penalty finite element method with discontinuous elements. SIAM J Numer Anal 1982;19:742-60. http://dx.doi.org/10.1137/0719052.
- [27] Underwood P. Dynamic relaxation. Comput Methods Trans Anal 1983;245-65.
- [28] Anderson T. Fracture mechanics: fundamentals and applications. CRC Press; 2017.
- [29] Wong T-f, Baud P. The brittle-ductile transition in porous rock: A review. J Struct Geol 2012;44:25–53. http://dx.doi.org/10.1016/j.jsg.2012.07.010.
- [30] Wawersik WR, Brace WF. Post-failure behavior of a granite and diabase. Rock Mech 1971;3(2):61-85. http://dx.doi.org/10.1007/BF01239627.
- [31] Wawersik W, Fairhurst C. A study of brittle rock fracture in laboratory compression experiments. Int J Rock Mech Min Sci Geomech Abstr 1970;7(5):561–75. http://dx.doi.org/10.1016/0148-9062(70)90007-0.
- [32] Ortiz M, Pandolfi A. A variational Cam-clay theory of plasticity. Comput Methods Appl Mech Engrg 2004;193:2645–66. http://dx.doi.org/10.1016/j.cma. 2003.08.008.
- [33] Radovitzky R, Ortiz M. Error estimation and adaptive meshing in strongly nonlinear dynamic problems. Comput Methods Appl Mech Engrg 1999;172:203–40. http://dx.doi.org/10.1016/S0045-7825(98)00230-8.
- [34] Ortiz M, Stainier L. The variational formulation of viscoplastic updates. Comput Methods Appl Mech Engrg 1999;171:419–44. http://dx.doi.org/10.1016/ S0045-7825(98)00219-9.
- [35] Drucker DC, Prager W. Soil mechanics and plastic analysis or limit design. Quart Appl Math 1952;10(2):157-65, URL http://www.jstor.org/stable/43633942.

- [36] Wei Y, Anand L. On micro-cracking inelastic dilatancy, and the brittle-ductile transition in compact rocks: A micro-mechanical study. Int J Solids Struct 2008;45(10):2785–98. http://dx.doi.org/10.1016/j.ijsolstr.2007.11.028.
- [37] Brace WF, Paulding Jr BW, Scholz C. Dilatancy in the fracture of crystalline rocks. J Geophys Res (1896-1977) 1966;71(16):3939–53. http://dx.doi.org/10.1029/JZ071i016p03939.
- [38] Brace WF. Volume changes during fracture and frictional sliding: A review. Pure Appl Geophys 1978;116(4):603–14. http://dx.doi.org/10.1007/BF00876527.
- [39] Robertson EC. Experimental study of the strength of rocks. GSA Bull 1955;66(10):1275–314. http://dx.doi.org/10.1130/0016-7606(1955)66[1275:ESOTSO] 2.0.CO:2.
- [40] Baud P, Schubnel A, Wong T-F. Dilatancy, compaction, and failure mode in Solnhofen limestone. J Geophys Res 2000;105(B8):19,289–303. http://dx.doi.org/10.1029/2000JB900133.
- [41] Ortiz M, Pandolfi A. Finite-deformation irreversible cohesive elements for three-dimensional crack-propagation analysis. Internat J Numer Methods Engrg 1999;44:1267–82.
- [42] Geuzaine C, Remacle J-F. Gmsh: a three-dimensional finite element mesh generator with built-in pre- and post-processing facilities. Internat J Numer Methods Engrg 2009;79(11):1309–31. http://dx.doi.org/10.1002/nme.2579.
- [43] https://supercloud.mit.edu.
- [44] Reuther A, Kepner J, Byun C, Samsi S, Arcand W, Bestor D, Bergeron B, Gadepally V, Houle M, Hubbell M, Jones M, Klein A, Milechin L, Mullen J, Prout A, Rosa A, Yee C, Michaleas P. Interactive supercomputing on 40 000cores for machine learning and data analysis. In: 2018 IEEE high performance extreme computing conference. HPEC, IEEE; 2018, p. 1–6.
- [45] Hunter JD. Matplotlib: A 2d graphics environment. Comput Sci Eng 2007;9(3):90-5. http://dx.doi.org/10.1109/MCSE.2007.55.
- [46] Ahrens J, Geveci B, Law C. Paraview:an end-user tool for large data visualization. Elsevier; 2005, http://www.paraview.org.
- [47] Ayachit U. The paraview guide: a parallel visualization application. Kitware; 2015, http://www.paraview.org.
- [48] Rice J. Mathematical analysis in the mechanics of fracture. In: Liebowitz H, editor. Fracture: an advanced treatise. Vol. 2, Academic Press; 1968, p. 191–311.